Overview of ASDEX Upgrade Results

O. Gruber for the ASDEX Upgrade Team*

Max-Planck-Institut für Plasmaphysik, EURATOM Association-IPP, Garching, Germany
* ASDEX Upgrade Team: see last page

E-mail contact of the main author: gruber@ipp.mpg.de

Abstract

During the last two years on ASDFEX Upgrade the physics base for ITER operation was significantly extended in both the foreseen standard H-mode scenario as well as the stationary improved H-mode scenario with enhanced performance. For anomalous transport (energy, particles, toroidal momentum) a multi-faceted picture of mode dominance in different plasma parameter regimes of ITG, TEM and ETG turbulence is evolving based on detailed measurements including fluctuation reflectometry and gyrokinetic calculations. Similar structures were found for natural and pellet induced, mitigated type I ELMs. They develop to outward drifting helical filaments which are seen as footprints on structures. New insights were gained on the interaction of energetic particles (driven by NBI and ICRH) with large scale instabilities (TAEs, NTMs, ELMs) based on new diagnostic and theoretical tools. The unexpected broadening of NBI driven currents beyond a certain heating power can be explained by a fast particle diffusion driven by small-scale turbulence. The active control of MHD instabilities (sawteeth, NTMs) concentrates on ECCD as proposed for ITER. NTMs were completely stabilized with very localized deposition of dc ECCD in improved H-modes, while for the deposition widths larger than the marginal island size as in ITER modulated injection phased with the island O-point was demonstrated to be advantageous. The tungsten coverage of the vessel interior was further extended up to 85%, where the highest erosion occurs at the LFS poloidal limiters, where it is dominated by ICRF accelerated impurities and fast particles from NBI. The W concentration can be kept at an acceptable level by ELM pace-making (using pellets) and by tailored central heating. The stationary improved H-mode extends ITER operation beyond its standard H-mode performance for confinement and beta with $H_{98(y,2)}\beta_N/q_{95}^2$ up to 0.4 (ITER reference value 0.2). Based on ASDEX Upgrade kinetic profiles it promises either a fusion performance up to ignition at full current or long pulses of up to 1 hr at reduced current (hybrid scenario). This operation mode extends well into the ITER dimensionless parameter range. Besides the development of discharge scenarios, the influence of the edge pedestal on confinement and of the flat central q profile on MHD and confinement was documented.

1. Introduction

The ASDEX Upgrade (AUG) device is a medium size divertor tokamak (R=1.65 m, a=0.5 m) with an ITER-like configuration, high shaping capability (single null and double-null divertor, elongation up to 1.8, triangularity d up to 0.5) and a versatile heating system. This consists of NBI (10 MW at 60 keV, 10 MW at 93 keV including 5 MW tangential off-axis deposition), ICRH with reliable operation up to 6 MW and type I ELM-compatibility using 3 db-couplers, and a 140 GHz ECRH (installed power 2 MW).

The AUG programme continues to strongly support ITER [1] and is conducted in close collaboration with our EU partners. During the last two years the physics base for ITER operation was significantly extended in both the foreseen standard scenario (transport, control of MHD modes, disruption mitigation, fast particle physics, full covered tungsten wall and divertors) as well as attractive scenarios with improved performance (improved H-mode, non-inductive current drive). Moreover, physics issues with impact beyond ITER, i.e. for future power plants such as DEMO, have already been identified and addressed. This is accompanied not only by development of the relevant technologies in diagnostics, heating and current drive, but also in control system.

In this respect a technical highlight in 2005 was the successful commissioning of a new integrated control and data acquisition system that is specially adapted to ITER needs with its machine-independent design, its integrated protection functions and the large number of real-time diagnostics and control functions [2]. This extremely flexible system responds to specific plasma states and allows the goal of the experiment to be achieved or to switch to alternative less ambitious or safe discharge scenario during a pulse. It is now in routine use at ASDEX Upgrade [3]. Presently the ECRH system is being enhanced to 4 MW /10 s pulse length at frequencies between 105 and 140 GHz and with poloidally steerable launchers for controlled

deposition during shots [4]. The comprehensive diagnostic system and its extensions are addressed in the paper.
In this overview, the recent progress is highlighted including the conclusions for ITER. Special emphasis is put on the high-Z wall programme with 85% tungsten coverage in AUG and the integrated improved H-mode scenario [5] with performance well beyond the ITER baseline scenario.

2. Core transport, turbulence theory and turbulence measurements

Understanding of anomalous transport is increasing, comparing the observed response of different transport channels on varying electron and ion heat fluxes and predictions based on the theory of core plasma turbulence [6]. Turbulent transport shows a multi-faceted picture of mode dominance of ion temperature gradient (ITG), trapped electron mode (TEM) and electron temperature gradient (ETG) turbulence in different plasma parameter regimes.
For purely electron heated plasmas the existence of a threshold in the normalized logarithmic temperature gradient $R/L_{Te}\approx 3$ was established when the electron heat flux tends to zero [7]. Now the explicit evidence of this threshold is provided by transitions from below to above the threshold at low ohmic heating power (I_p=400 kA) [8]. Combinations of on- and off-axis ECRH were used, while keeping the total electron heat power constant. Linear calculations with GS2 found a dominating TEM turbulence and the same heat flux dependence upon R/L_{Te}. [9]. The results are presented in Fig. 1 together with results from empirical transport modelling and GS2. This power balance result was confirmed by simultaneous heat pulse propagation analysis. The jump like increase of both χ_e^{amp} and χ_e^{phase} around the threshold shows consistent evidence of the transition through the threshold.

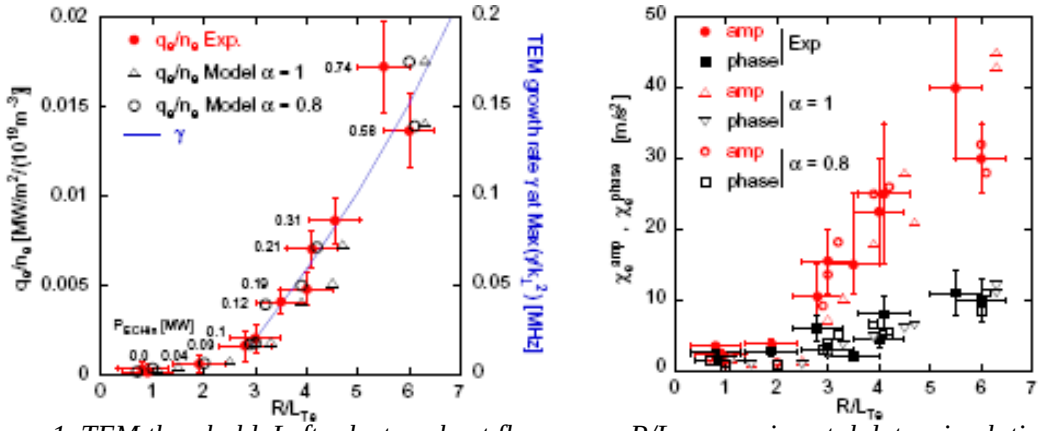

Figure 1. TEM threshold. Left: electron heat flux versus R/L_{Te}, experimental data, simulations with empirical model and growth rate of the TEM.
Right: χ_e^{amp} and χ_e^{phase} versus R/L_{Te}, experimental and modelling data.

The observed flattening of the density profile with increasing collisionality on AUG [10], JET and TCV [11] is roughly consistent with a transition from dominant TEM to dominant ITG turbulence [12]. This explanation is based on predictions of the gyrofluid model GLF23, but is in some disagreement with nonlinear gyrokinetic GS2 code results [13]. The stabilization of the TEM due to collisions and the transition to ITG turbulence [14] has been demonstrated by heat pulse studies with increasing density. This is a combined effect of the increasing collisionality and the decrease of T_e/T_i. [8]. This transition from TEM to ITG dominance with increasing collisionality is also observed in the particle transport behaviour [15,16].
A strong link between ion heat and momentum transport on AUG was found experimentally [18]. Assuming diffusive laws for T_i and v_Φ. a strong correlation between χ_Φ and χ_i-$\chi_{i,neo}$ was quantified by power balance analysis using the ASTRA code. The ratio $\chi_\Phi/(\chi_i-\chi_{i,neo})$ decreases from 1.2 to 0.7 across the radius. These experimental results are in promising agreement with recent estimates from linear gyrokinetic calculations for ITG instabilities [19].

In contrast to neoclassical transport leading to impurity accumulation driven by background density gradient (increasing with Z) [20], turbulent transport involves no strong central impurity accumulation [14,21]. Under experimental conditions an outward pinch exists (ITG turbulence), which can explain the suppression of high-Z impurity accumulation by applying central auxiliary heating (see Sect. 7) [22,23]. This should also maintain for ITER with central α-heating.
Microinstabilities are affected by the radial gradient of the ExB velocity responsible for the shear flow stabilization. E_r profiles, its radial shear and its fluctuations are directly measured by Doppler reflectometry using the correlation technique and the results are compared to plasma turbulence [24,25,26]. In the plasma edge the notably robust E_r radial profile shows a narrow negative well coinciding with the steep pedestal pressure gradient whose depth scales with the plasma confinement: from typically -5kV/m in ohmic & L-mode conditions to -30 kV/m in H-modes, to over -50 kV/m in improved H-modes [26]. The core E_r in ohmic discharges reverses from positive to negative together with a transition in the dominant turbulence from TEM to ITG when the collisionality increases [16].

3. Edge transport barrier physics and ELMs
Type I ELMs release a substantial amount of particles and energy to the first wall and divertor. They remain a major problem for the target lifetime in ITER [28]. Based on the global characteristics and detailed parameter studies found on AUG, empirical scalings have been deduced as well as extrapolations towards ITER [29,30]. Concerning the ELM energy losses and the ELM loss power fractions, those are comparable in improved and standard H-modes [31]. Regimes with small, high-frequency ELMs, similar to grassy ELMs at high poloidal β in JT-60U, were obtained in AUG in configurations near double null [30]. This grassy ELM regime, which occurs at high edge safety factor and medium edge collisionality, was compared to the type II regime [32,33] obtained with strong shaping and also near double null [30].
On AUG we have developed active tools for ELM mitigation, where the ELM pacing by quasi-continuous cryogenic hydrogen pellet injection is the most promising one [34,35]. In fact, this method is routinely applied, as for instance in radiative edge discharge scenarios with noble gas injection to enforce regular ELMs (see Sect. 7) [36]. The structure and dynamics of natural and pellet induced ELMs, as well as the related wall effects are compared in [37,38]. This is based on an extensive set of fast edge diagnostics, as fixed arrays of magnetic and Langmuir probes [39], a reciprocating Langmuir probe, 2d Thomson scattering snapshots [40], reflectometry, thermography [41,42] and video cameras [43]. The event sequence and the physical mechanisms during different ELM cycles are similar. Initially weakly correlated, magnetic field-aligned, attached helical structures start in the pedestal with a broad spectrum of medium ($n \leq 8$) effective toroidal mode numbers. Those develop to fully detached, approximately electrostatic, outward drifting filaments in the scrape-off layer wing with $n \approx 8$-24. These filaments are seen as footprints on the LFS limiters [42,44] and on the divertor targets [41] as non-axisymmetric spiral structures by thermography. The triggered ELMs are released once the pellet has penetrated up to the pedestal top. The basic signatures of induced ELMs are rather similar to those of spontaneous ones as is the ELM affected plasma area. The comparison with theoretical ELM models , e.g. [45], is still going on.

4. Fast particles: losses by MHD modes and redistribution by turbulence
In view of ITER, we extended our efforts to study the interaction of fast particles with large scale magnetic perturbations and small-scale turbulence which impacts heating and current drive efficiency and wall loading [46]. The flexible heating system of AUG allows the effects of bulk plasma and fast ion population to be separated. TAE damping rates, determining the amplitude of fast-particle excited TAEs and hence the associated losses, showed high values at JET [47]. The dominating TAE damping mechanism may be explained by an intersection of the TAE frequency and the continuum Alfvén spectrum at the plasma edge. The coherence

profiles of magnetic and fluctuation reflectometry signals of ICRH excited TAEs show good agreement with the calculated eigenfunctions using the linear global gyrokinetic eigenvalue code LIGKA [48] with measured edge densities [46, 49].
New insights have been gained using a new fast ion loss detector (FILD, with a bandwidth of 1 MHz using photomultipliers) for energy and pitch-angle resolved distributions of the lost particles [50]. For the first time it was not only possible to identify directly the frequency and phase correlation of fast ions with TAEs (excited by beam injection or ICRF beat waves) [45,51], but also for low frequency MHD activity (NTMs, double tearing modes, ELMs). Together with the modelling of the particle orbits the mechanism of fast particle losses due to these helical perturbations can be found.
NTMs leading to large islands drive losses to the detector, which are modulated with the rotating mode and in fixed phase relation (Fig. 3). Fast switching of the beam sources with different injection angles and energies gives information on the origin of the fast particles and their loss rate. Losses occur within 100-1000 toroidal orbit transits due to stochasticity of overlapping drift islands. The losses decrease when the NTM is actively stabilized with ECCD (see sect. 5). Observed large fast ion losses caused by magnetic islands correspond to enhanced heat loads to the limiters.

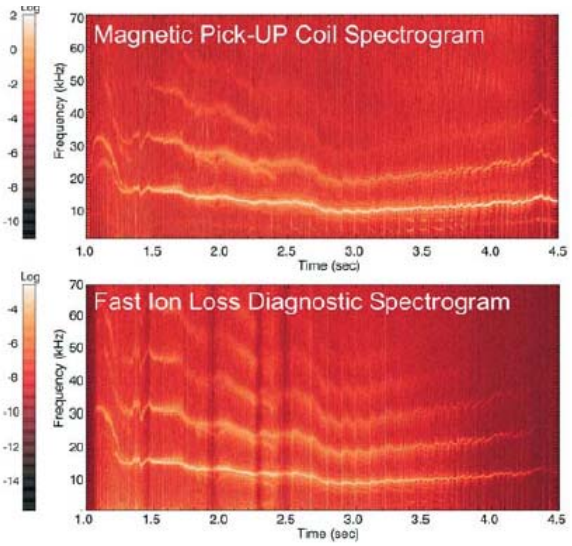

Fig.3 : NTM (magnetic signals, ~5-20 kHz and harmonics) induces fast particle losses measured by fast ion loss detector.

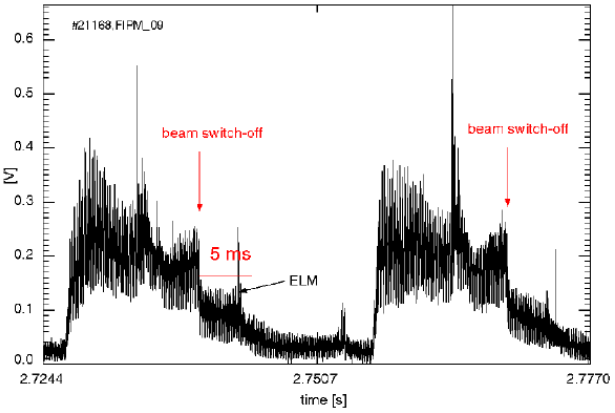

Fig. 4: Response of the fast ion losses to switch-on and –off of the NBI source for particles deposited on the low field side

The FILD signal of a double tearing mode event is shown in Fig. 4. NBI particles, ionized at the low field side outside the separatrix, respond immediately to the NBI switch-off. Co-injected particles deposited inside the separatrix on the LFS reach the detector only after drifting of the orbits to the outer flux surfaces, which takes about 5 ms. This delay can be explained by drift orbit calculations due to a region of orbit stochasticity. It is also limited by the collisional slowing-down of the fast particles.
Current drive experiments on AUG with off-axis beams show beyond a certain power level, which increases with shape triangularity, a marked broadening of the driven current profile [36], while the total driven current, as derived from the loop voltage, agrees well with TRANSP predictions. This shift of the off-axis injected current towards the axis cannot be explained by current diffusion. The parallel electric field (derived from equilibrium reconstructions with CLISTE using MSE and loop voltage measurements [52]) immediately responds to a change from on- to off-axis or reverse, but flattens again within 100 ms. MHD activity and Alfvén waves can be ruled out. Only the current source itself, the fast particles, can be redistributed on this time scale. This could be modelled in TRANSP by assuming a diffusive redistribution of the NBI ions with a modest diffusion coefficient of about 0.5 m^2s^{-1}.
The correlation with the turbulent thermal heat transport has led to the suspicion, that small-scale turbulence driven by thermal plasma parameter gradients might also act on supra-thermal particles. A linear global gyrokinetic turbulence code was developed to include fast

particle orbits and the effect of background plasma turbulence on the fast particle dynamics. Indeed, direct numerical simulation of fast test particles in an electrostatic turbulence field indicate that fast and thermal particle diffusion are similar for reasonable parameters [46]

5. Control of MHD instabilities by ECCD:

The active control of performance limiting sawteeth and NTMs concentrates on ECCD as a control tool with its flexible and localized deposition. In ITER the sawtooth control and suppression of NTMs is even necessary for the reference scenario [1]. Pioneering work was done at AUG for NTM stabilization so far, namely tearing mode stabilization by dc ECCD injection into the island (in 1998) [53] and detection of FIR-modes leading to self-stabilization by coupling to higher modes (in 2001) [54,55]. The requirements for the ECCD control emphasize the localization of the ECCD current, i.e. maximum I_{ECCD}/d^2, where d is the radial half width of the injected ECCD. Either the equilibrium current profile is changed (sawteeth) or helical currents are generated within the island of the resistive MHD mode (NTMs) [56]. For the NTM stabilization with very localized ECCD deposition, W/(2d)>>1 (island width W), dc ECCD is as effective as ECCD modulated in phase with the island O-point. But the effectiveness of dc ECCD decreases when 2d becomes larger than the island width W and the stabilization term saturates while the destabilizing bootstrap drive behaves like β_p/W. Theory predicts that the stabilizing term can then be enhanced by modulating the ECCD source in phase with the island O-point, while for X-point modulation the helical current is destabilizing. The verification of these theoretical predictions and the implications for ITER are discussed in [56].

The beneficial effect of very localized dc ECCD deposition for NTM control was documented by changing of the toroidal launching angle Φ which allows via the variation of the deposition zone the modification of the ECCD width d (Fig 4). Maximizing $\eta_{NTM}=j_{ECCD}/j_{bs}$ with $j_{ECCD}\sim I_{ECCD}/d$ at injection angles around Φ=5° allows complete stabilization of both (3,2) and (2,1) NTMs and a significant increase of the β_N range at small deposition widths (W/(2d)>1) (Fig left). At broader deposition widths with W/(2d)<1 (Φ>15°) only partial stabilization is achieved with dc ECCD [55]. Fig. 5 summarises stabilization experiments at similar plasma parameters where the figure of merit, H/H(noECCD), characterizes the confinement increase due to stabilizing of the (3,2) NTMs (confinement factor H is based on the IPB98(y,2) scaling). It is lowest for cases where the full ECCD deposition 2d exceeds the island size (left corner) and increases with stronger localisation of the ECCD current. The normalization to T_e/n_e accounts for variations in the current drive efficiency due to varying plasma parameters.

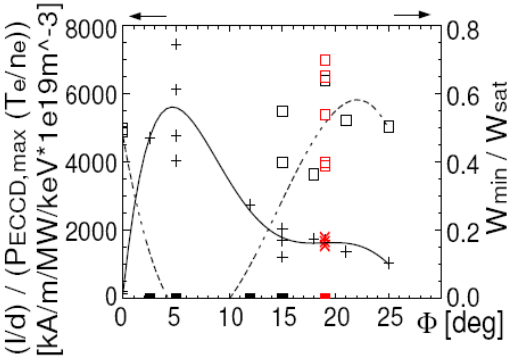

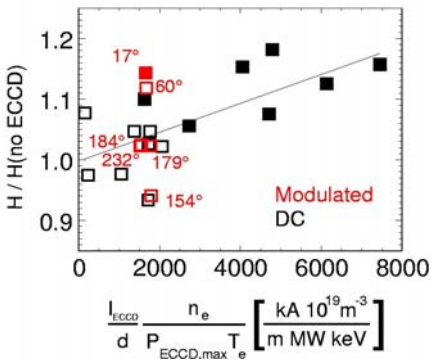

Fig. 4 : Normalized ECCD current density I_{ECCD}/d (from TORBEAM calculations) as a function of the toroidal launching angle Φ (black crosses) together with the experimentally achieved normalised minimal island size Wmin/Wsat of (3/2)-NTM.
Black squares: dc injection, red squares: modulated injection. Full symbol: full stabilization. Open symbol: partial stabilization. The red numbers indicate the phase of the modulated ECCD relative to the island O-point.
Fig. 5: The relative increase in confinement factor H due to (3,2) NTM stabilization under a variation of the ECCD deposition widths. The same data set as in Fig. 4 is used.

New results from modulated ECCD for a broad deposition with W/(2d)=0.6 (on/off modulation with 50% duty cycle) are also shown in Fig. 4 and 5. They demonstrate the advantage of injection close to the O-point (at 17°), whereas X-point modulation (at 154°) reduces the efficiency below the dc values in agreement with the theoretical picture. With modulation the average power can be used more efficiently [57].
These experiments with an artificially broadened deposition profile mimic the situation in ITER, where the deposition width d will be larger than the marginal island size which scales like the normalised poloidal ion gyroradius. Under these conditions on AUG complete stabilization cannot be achieved any longer using dc injection at 1.1 MW ECCD. But modulated injection phased with the rotating island O-point achieves complete stabilization. This implies important consequences for ITER: The ECCD system should be optimized for narrow deposition, and the gyrotrons should enable phased injection with the frequency of the rotating islands. The required power is presently extrapolated using a multi-machine database [58].
The next steps on AUG concentrate on the on-line determination of mode position as well as ECCD deposition to steer the ECCD antenna mirrors for deposition control in the framework of the extension of the ECCD system to 4 MW, 10 s, with variable frequency [59].

6. Disruption mitigation using fast impurity puffs

Besides the localized divertor heat loads with type I ELMs, the heat loads as well as the force loads from disruptions are a concern for ITER and even more for DEMO [1, 28]. In addition the generation and consequent deposition of runaway electrons has to be avoided. All three detrimental disruption effects may be considerably reduced by the massive injection of impurity gas before the thermal quench occurs [60]. Beyond the investigation of the underlying physics and the development of fast gas valves [61], we routinely use the fast injection of neon for plasma shut-down [62]. The injection was formerly triggered by a neural network predicting a disruption based on real-time diagnostics and more recently by a locked mode magnetic signal, and leads to the onset of a mitigated disruption within a few milliseconds. Mitigation based on gas injection is advantageous compared with the earlier applied impurity killer pellets as no cryogenic system is needed for gaseous impurities and the runaway production is negligible.
The impurity gas should cool the plasma by dilution and radiation before the thermal quench is caused by MHD instabilities and, for vertically unstable elongated divertor plasmas, should accelerate the current quench to limit the vertical plasma shift and the connected force. On AUG the number of injected impurity atoms is close to the plasma inventory, but, as in other tokamaks [63], most of them do not penetrate deep and before the thermal quench. Cooling happens due to a radiating cold high density mantle. The force mitigation is robust by a factor of 2-3 and halo currents as well as currents in the stabilizing loop are equally reduced. The force reduction is well correlated with a reduced maximum vertical plasma excursion. This is less due to a significant shorter current quench but caused by a modified vertical displacement dynamic. As the measured force reduction increases with the gas amount, a new valve is being developed with a high gas reservoir, which is kept under high pressure up to 50 bars.

7. Tungsten as first wall material

High-Z walls will be crucial for future machines in view of sputtering and the tritium trapping in carbon walls. Especially in DEMO the erosion of low-Z material and the destruction of graphite under neutron bombardment will be unacceptable [64,65]. The main risk using tungsten is a strong central radiation loss, and the tungsten concentration has to be kept below a level of about 10^{-4}. In fact the central peaking of the main ion density can cause inward drift of high-Z impurities as predicted for neoclassical transport [20,22,23]. These inward drifts due to density gradients in the H-mode edge barrier and in the core plasma have to be compensated.

Since the last IAEA in 2004 the coverage of the AUG vessel interior with Tungsten was further extended up to 85% (36 m^2) with the coating of the poloidal limiters at the low field side which receive the highest load in the main chamber [66,67]. The complete coverage is being done in the present shut-down, namely the coating of the the lower LFS divertor targets. To prevent the higher force loads due to eddy currents induced in tungsten compared with graphite, we have chosen the solution of W coating on graphite. Thin coatings of <5 μm are used throughout (physical vapour deposition) except for the strike point regions of the lower divertor targets, where 200 μm coatings by vacuum plasma spray are used.
With increasing tungsten coverage a clear reduction of the carbon concentration was seen, which is, however, less than proportional to area reduction (Fig. 6a) [68]. Modelling of the C particle transport and the migration pattern including main chamber recycling can describe the C evolution. A net carbon source of 1.5 $\times 10^{19}$ atoms/s from the outer divertor has to be assumed (Fig. 6b). Local flux measurements from the HFS and LFS walls and fast reciprocating Mach probe measurements support this model. According to this, we should get rid of carbon in the next campaign with full W covering of the divertor. Then carbon will not be available as radiator in the divertor any longer. Replacing it by argon seeding and in combination with type-I ELM pacemaking at sufficiently high frequency a cold divertor regime was already established in between ELMs (H-factor above 1) [36,69].

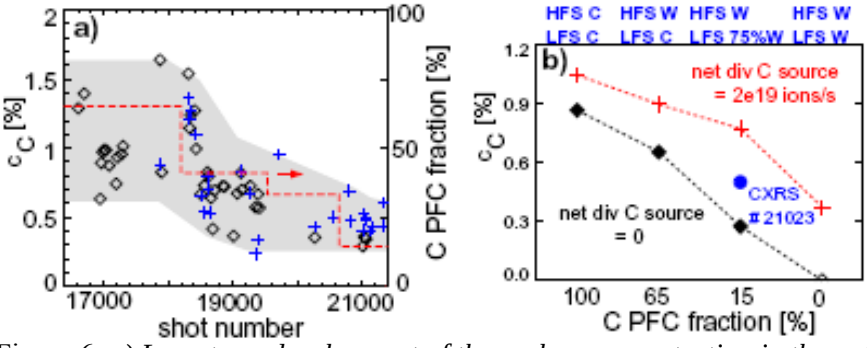

Figure 6: *a) Long term development of the carbon concentration in the outer core plasma during a high density standard H-mode phase as measured by CXRS with NBI injector 1(diamonds) and 2 (crosses). The dashed lines indicate the fraction of PFC carbon coverage. b) Modelling of the C concentration with changing W coating in AUG with and without net C ion influx from the divertor.*

The increase of W-coated areas is also reflected in an increase of the W content. However, the W concentration could be kept in the range or below 10^{-5} over broad range of discharge scenarios [66]. Fig. 7 shows the distribution of the W concentrations for the last three years. The large variation of the W concentrations reflects the fact that the W transport is influenced much more by the plasma conditions than the carbon concentration. The control measures taken include both the reduction of central W impurity accumulation by tailored central heating with waves (ICRH, ECRH), as well as the control of the impurity flux across the ETB by ELM pace-making using cryogenic pellet injection. High ELM frequency needed for shielding of high Z-atoms is required anyway for reduced ELM energy deposition (target lifetime!). The necessary central heating at a level comparable to the envisaged ITER values increases the turbulence and hence the impurity particle diffusivity, which is connected with the core heat flux, but is also perceived by reduced hydrogen density peaking. The two colours of the distributions in Fig. 7 represents two subsets of the data with (red) and without (black) considerable ICRF heating [67]. Without ICRH the distributions are very similar, while with ICRF the mean value of the tungsten concentration increased by a factor of 5 in the last campaign with the W-coating of the LFS limiters (see below). No problems are encountered with ITER scenarios at high edge densities needed for exhaust. However specific discharge scenarios, which are orthogonal to the requirements identified for low tungsten erosion and sufficient core transport, are hampered without boronization, e.g.: high core confinement, high temperature at plasma edge, low ELM frequency and predominantly off-axis heating.

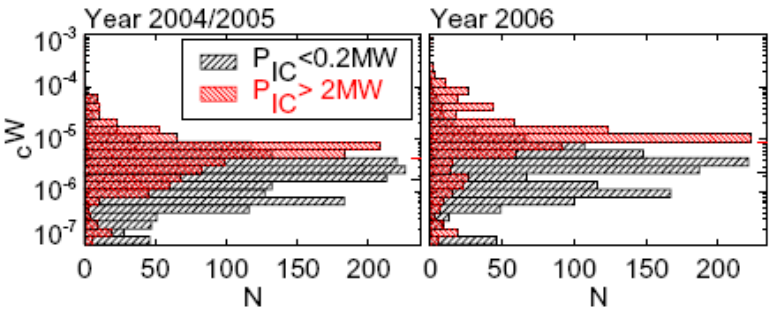

Figure 7: Distributions of tungsten edge concentration with(red) and without(black) considerable ICRF heating for the campaign 2006 with tungsten limiters in comparison to two previous campaigns with graphite limiters. Bars at the right hand side give mean values[67].

The last enhancement for the campaign 2006 of the W covering focused on the poloidal limiters at the low field side. For the tungsten erosion at the these limiters, fast particles from NBI as well as impurity ions accelerated in the rectified sheath in front of the active ICRF antennas have been shown to play an important role, while CX neutrals yield only a minor contribution. Local W-flux measurement on the limiters with high time resolution (even ELMs can be resolved) allowed detailed conclusions [70].
Fast deuterium ions from the NBI sources are transported to the LFS limiters during the slowing-down and sputter tungsten there. Experimental results of the tungsten erosion rates using NBI sources with different injection angles can be modelled with the fast particle load as derived from Monte-Carlo calculations. Extrapolations to ITER based on calculated birth profiles of α-particles and beam ions, taking into account the expected ripple, suggest that the W-erosion by these fast particles should not be critical.
When ICRF is switched on/off, the tungsten influx from the limiters of the ICRF antennas strongly inceases/decreases on a sub-ms timescale. Compared with NBI the local W influx densities are up to a factor of 65 higher at the same heating power [70]. The fast temporal response and the spatial structure rule out a dominant effect from ICRH produced fast plasma ions, but point to sputtering by impurity ions accelerated at the antenna by sheath rectified E-fields. Empirically it was found that 2-strap antennas reduce the W-influx, and the effect of the faraday screen is weak. Fresh boron layers survive only a limited number of discharges at the LFS limiters [71]. The reduction of W-peaking during central ICRH is still valid, but the increased W-source overrides the beneficial effect resulting in higher W-concentrations with ICRH [66]. Consequently central ECRH is the preferential choice. In H-modes with type-I ELMs, about 70% of the local W-influx at the middle of an ICRF limiter appears during ELMs independently of the ELM frequency. During the ELM, the mean energy of the ions hitting the W-surface is increased as indicated by the increased sputtering yield, which is the predominant contribution to the rise of the tungsten influx [70].
Changes in the total gas balance are not yet detectable, however, the release of short term retained noble gases in the tungsten coated tiles shows a pronounced increase with respect to the pure graphite tiles. After He glow-discharge cleaning, a large release of the stored He occurs, as was shown by spectroscopic measurements. This effect is confirmed by laboratory experiments [72]. The frequency and duration of He glow discharges, which were routinely performed after each discharge, was reduced [73].

8. The Improved H-mode: Operation beyond the ITER baseline scenario

The improved H-mode, discovered at ASDEX Upgrade in 1998 [5], demonstrates the integration of advanced performance beyond the standard H-mode at improved confinement ($H_{98(y,2)}$~1.1-1.5) and enhanced stability (β_N~2.5-3.5) under stationary conditions even with respect to current diffusion [5,74,75,76]. Its performance potential in terms of $H_{98(y,2)}\beta_N/q_{95}^2$ up to 0.4 (ITER reference value 0.2) is combined with the robustness of ELMy H-mode operation and contrasts with advanced scenarios based on internal transport barrier (ITB) discharges with strongly reversed q-profiles, which are not stationary at comparable

performance up to now. This regime is the candidate for the ITER hybrid scenario, which aims at reduced plasma current to long pulse lengths with dominating a-particle heating ($Q\approx10$, $H_{98(y,2)}\beta_N/q_{95}^2\approx0.2$) [76,77]. Alternatively, at full plasma current, the performance can exceed the base line values of $H_{98(y,2)}\sim1$and $\beta_N\sim2$, giving conditions close to ignition at still extended pulse lengths above 400 s ($H_{98(y,2)}\beta_N/q_{95}^2\approx0.4$).
To date, the ingredients essential for improved H-mode operation are still being investigated as well as the reason for the observed confinement and stability improvements and the differences compared to standard H-modes. In contrast to the standard H-mode with $q_0<1$ and the ITB discharges with reversed q-profile, the q-profiles of the improved H-mode are flat with low magnetic shear in the centre ($q_0\geq1$) avoiding sawteeth. Typically, this q profile is achieved by early heating with moderate NBI power during the current rise phase to slow down the current diffusion. This is followed by strong heating in the flattop phase up to high β_N, because seed islands for detrimental (3,2) NTMs are absent without sawteeth. Finally the onset of (2,1) NTMs limits the β value. The flat q profile is sustained by mild central MHD activity, often (1,1) fishbones or small NTMs with higher mode numbers $m/n\leq3/2$ [75,76].

8.1. Influence of discharge scenarios on performance

While the ramp-up in AUG was initially done in a high-field-side limiter configuration (1998-2002), this scheme had to be changed with the tungsten coating to a ramp-up in a divertor configuration allowing for lower plasma densities and a control of the impurity content. The limiter ramp-up resulted in general in a central (1,1) fishbone activity [5,79], whereas the divertor ramp-up mainly shows small (5,4), (4,3) and finally weak (3,2) NTMs [76]. Thereby the discharges with fishbone activity displayed higher performance values. Recently, improved H-modes have also been obtained with "late" additional heating well in the current flattop which partly show even better performance (higher plasma energy and H-factor, e.g. $H_{98(y,2)}\sim1.5$ as compared to 1.2-1.3 for the early-heating scheme) [79].

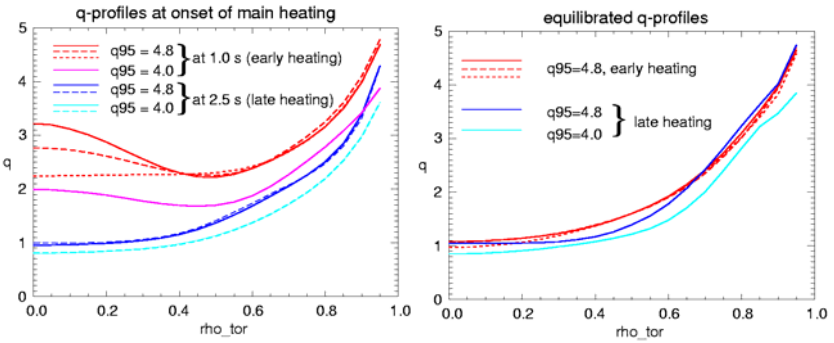

Fig. 8: Variation of q-profiles at the onset of the main heating (left) and equilibrated current profiles (right) obtained by modification of the ramp-up phase. Red: early heating q_{95}=4.8, magenta: early heating q_{95}=4.0, blue: late heating q_{95}=4.8, cyan: late heating q_{95}=4.0.

For a systematic comparison of the two heating scenarios with identical discharge parameters (current, q95, density, shape) the evolution of the q profiles from the onset of the main NBI heating to the equilibrated current profile phase is given in Fig. 8. The q profile for the early-heating scheme (in divertor configuration) relaxes within 3 s from a profile with $q_{min}>2$ to a slightly peaked current density profile exhibiting during the central q drop first (4,3) and then (3,2) NTMs (Fig. 9). The late-heating scheme relaxes only slightly to a very flat q-profile ($q_0\geq1$) at the heating onset favouring the onset of a (1,1) fishbone activity (Fig. 9).

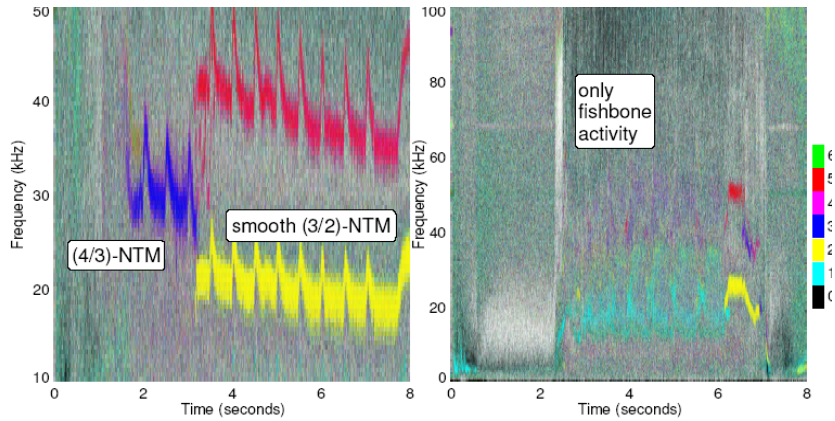

Fig. 9: MHD activity of early-heating (left) and late-heating (right) improved H-mode scenarios in divertor configuration. Colour code refers to toroidal mode numbers.

In this case both q-profile and fishbone activity resemble previous results with the early-heating scheme in a limiter configuration, and the better confinement is in accordance.
Obviously the current profile and /or the related MHD influence the transport properties. In terms of the energy confinement it is beneficial if even these weak NTMs can be avoided. In addition, the linear threshold of the inverse temperature gradient length R/L_{Ti} for the onset of ITG turbulence is proportional to the the magnetic shear normalized to q ($s/q=r\,\nabla q/q^2$). In the confinement zone the measured s/q and R/L_{Ti} values are higher in the late-heating scenario as are the critical R/L_{Ti} values calculated with the linear GS2 code [79]. Also the pedestal pressure is higher in the late-heating case (see discussion below) [31].

8.2. Confinement and edge-core relation

Stiff temperature profiles limited by drift-wave turbulence are observed in all H-mode discharges at AUG [80,81,82]. The corresponding linear relationship between core and edge temperatures leads to a linear relationship between total stored energy and pedestal pressure or pedestal energy within variations due to the density profile shape as shown in Fig. 10a [31]. Improved H-modes occur at higher plasma energies and, in accordance, they populate higher values of H (Fig. 10a). More peaked density profiles can occur with improved H-modes (see pulse 15651) but a clear correlation of confinement enhancement with density peaking is not found. In addition the usually applied central wave heating against impurity accumulation is also perceived by reduced hydrogen density peaking compared with former pure NBI heating cases [75,76]. The density peaking is decreasing with increasing density related to the Greenwald density.
A contribution to this improved confinement was found by enhanced pedestal pressures of the H-mode ETB which increase with input power [84,85]. The data base for this contribution is still limited at present, as dedicated pedestal profile measurements with high resolution are only available for discharge subsets [30,31]. Mainly the pedestal electron and ion temperatures increase compared with standard H-modes and contribute to the edge pressure increase (Fig. 10b) [31]. This is connected with a widening of the Te edge transport barrier, not an increasing gradient. The rough scaling of both the total plasma energy and the pedestal pressure increases stronger with input power in improved H-modes on AUG compared with the IPB H-mode confinement scaling ($W_p \sim P^{0.3}$; $\tau_E \sim P^{-0.7}$) [85].

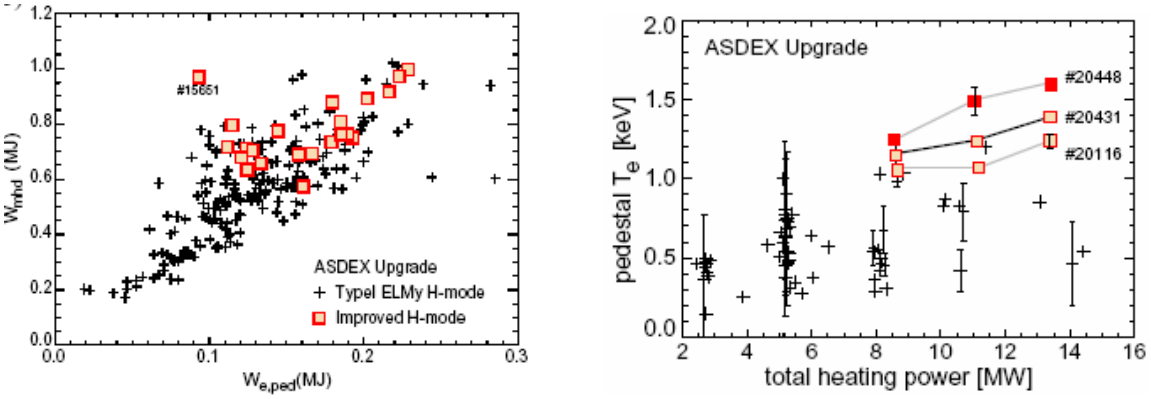

Figure 10: Edge-core relation in improved H-mode and type I ELMy H-mode data sets: (a) total MHD stored energy vs. pedestal electron energy. (b) Pedestal electron temperatures vs. heating power.

8.3. Operational range, beta limits and active NTM control

The dimensionless parameter range of the improved H-mode is demonstrated in Fig. 11 [86]. A dataset with all Type I ELMy H-modes stationary for more than 0.2 s, which may contain improved H-modes, and all improved H-mode discharges, according to our recipes and stationary for >0.5 s, are compared. On average improved H-modes achieve higher confinement factors and higher β_N compared to standard H-modes and allow a higher performance than the ITER reference scenario to be routinely achieved. Improved H-mode

discharges can be extended up to high divertor relevant densities, where the highest values of $<n_e>/n_{GW}$=0.85 with good confinement are obtained in a high triangular plasma shape (δ=0.4). Recent experiments have achieved $<n_e>$=1.1 1020 m-3 at 1 MA (q_{95}=4) with a moderately peaked density profile and still temperatures of 3 keV in the centre. Here the collisonality is a factor of 10 above the ITER reference value. But the operation at lower densities documents the reliable operation at ITER relevant ν* achieving the highest confinement factors.

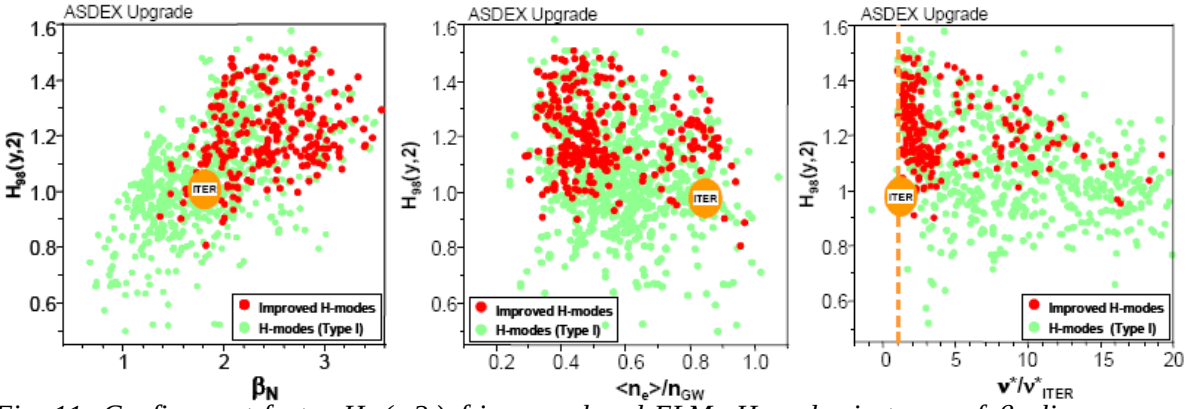

Fig. 11: Confinement factor $H_{98}(y,2,)$of improved and ELMy H-modes in terms of β_N, line averaged density normalized to Greenwald density ($<n_e>/n_{GW}$). and collisionality normalized to the ITER collisionality (ν^*/ν^*_{ITEP})

Improved H-mode discharges can achieve high $\beta_N \approx 3$ at all explored q_{95} values. The maximum beta values are near to the no-wall limit $\beta_N = 4l_i$ and are limited by a (2,1) NTM. The improved H-modes at low $q_{95}<3.5$ reach the highest β_N values (up to 3.5) and often show fishbone activity at high β_N. But these discharges are prone to spontaneously develop large (3,2) NTM modes above $\beta_N>2$. A characteristic feature of the (3,2) mode at these q values is that the impact on confinement is generally very pronounced, the H factor drops below 1 [56,86], in contrast to (3,2) modes at higher q_{95}. We attribute that to the fact that at lower q_{95} the (3,2) rational surface is located further out in a zone of steeper pressure gradients. Applying active control with dc ECCD and optimized narrow deposition in the island region the (3,2) mode can be stabilized (see Fig 12) and the discharge enters into good improved H-mode conditions with fishbone activity (indicated by the trace ´n=1 amplitude´ in Fig 12). Under these conditions the kinetic energy recovers to $H_{98(y,2)}$=1.15 and β_N rises up to 2.6. Without ECCD the (3,2) NTM stays, the confinement deteriorates, and finally a (2,1) NTM develops [86].

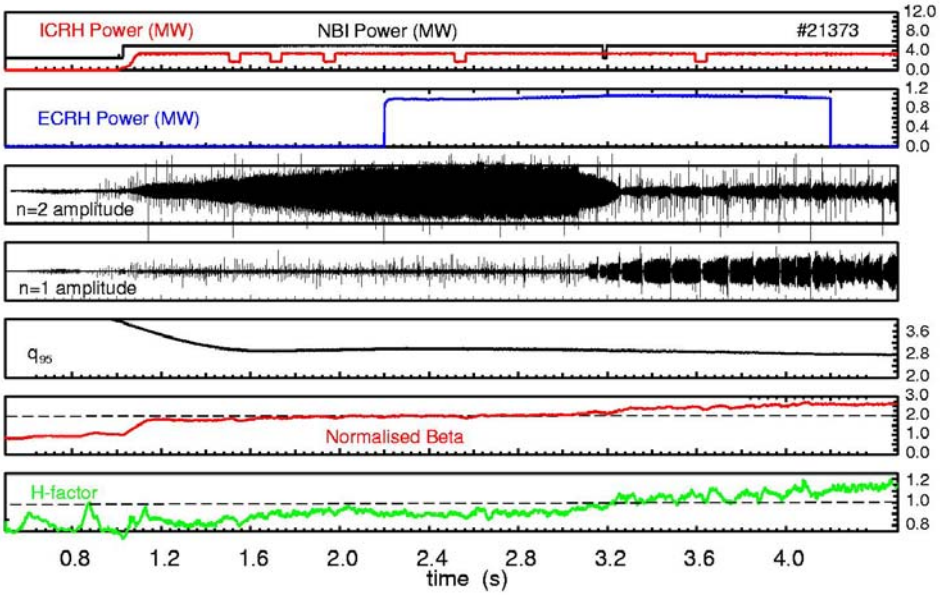

FIG. 12. Stabilization experiment of a (3,2) NTM by sweeping ECCD over the q=1.5 surface using a mild B_t ramp with a narrow deposition profile (W/(2d)=0.6) in an improved H-mode at q_{95} = 2.9.

8.4. Prospects for ITER operation

For the extrapolation to ITER the ASTRA transport code is used to predict the fusion performance from scaling the kinetic profiles measured in AUG for both conventional type I and improved H-modes [86]. The plasma current in ITER is chosen to match the q_{95} of the AUG discharges using B_t=5.3 T and the ITER plasma shape (14 to 9 MA for q_{95}=3.1-4.8). The density profile shape is kept and its value adjusted to $<n_e>/n_{GW}$=0.85. The shape of the temperature profiles in ITER (T_e=T_i) was taken from the AUG T_i and T_e profiles, respectively. The scaling factor for the T profiles is determined by the measured $\beta_{N,th}\approx$0.8-0.9 β_N, assuming that the same values can be achieved in ITER at lower normalized Larmor radius and in agreement with the first scaling experiments done at AUG [75,76]. Equal D and T densities are assumed, while the impurity concentrations and $Z_{eff}\approx$1.65 are taken from the ITER design. Standard H-mode discharges of AUG come close to the ITER reference (big green point in Fig. 13). The ITER fusion powers resulting from the scaled kinetic profiles of AUG improved H-modes range from 400 MW at I_p=9.4 MA (q_{95}=4.8) to 1070 MW at 14.2 MA (q_{95}=3.1) at β_N=2.6-2.8 as shown in Fig. 13. The lower plasma current represents a hybrid operation with Q≤10 and $f_{BS}\approx$0.4, whereas the higher current yields a fusion power in excess of 1 GW and Q=∞. Here the pedestal density of 7 10^{19} m^{-3} and temperatures of 5.7 keV are within the ITER design values. The estimated required input power depends on the confinement scaling law where IPB98(y,2) is used here and the $H_{98(y,2)}$ values are taken from the AUG discharges. Due to the strong beta degradation of this scaling some cases at higher β_N would need additional power in excess of the envisaged 73 MW especially for low currents and are indicated by open circles in Fig. 13. GyroBohm [87] or the "Cordey" [88] scaling (both $B_t\tau_E\sim\beta^0$) are much more optimistic for P_{aux} and hence Q.

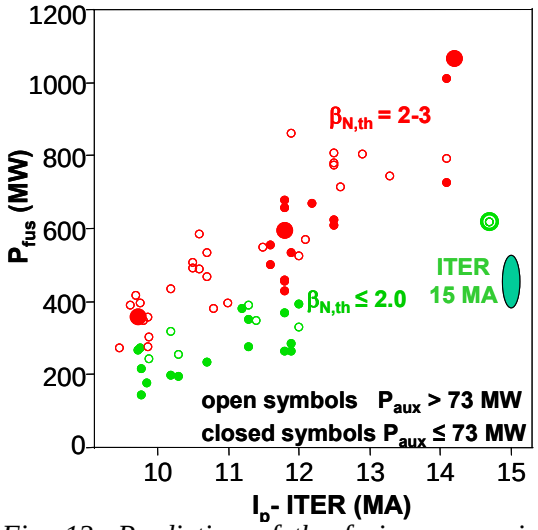

Fig. 13: Prediction of the fusion power in ITER from scaling up kinetic profiles data from ASDEX Upgrade. Input power requirements (P_{aux}) to sustain the β_N in ITER as obtained in ASDEX Upgrade for the IPB confinement scaling law.

9. Conclusions and Outlook

The AUG programme is mainly focussed on the development of consistent and integrated high performance scenarios for ITER. Part of it is the development of control tools and suitable actuators for stationary discharge scenarios, kinetic profiles and impurity content, as well as MHD control and ELM and disruption mitigation.

Substantial progress was made with high relevance for ITER. Concerning NTM stabilization the ITER reference parameters should be obtainable using modulated ECCD injection phased with the rotating island O-point and aiming at a small deposition. Our ECRF system is presently being upgraded in power (4 MW), pulse length (10 s) and deposition variability.

A central part of our effort is the development of the improved H-mode with its high potential to guide ITER beyond its reference parameters. At full current (q_{95}=3.1) a high fusion power for improved H-mode discharges is predicted ($H_{98(y,2)}\beta_N/q_{95}^2\approx$0.4). At lower I_p in ITER (9-11 MA), a significant fusion power can still be achieved at very long pulse lengths ($H_{98(y,2)}\beta_N/q_{95}^2\approx$0.2). The auxiliary power requirements at high β_N>2.5 and at I_p<11MA may exceed the maximum P_{aux} planned for ITER (73 MW). On AUG the operational range of this tokamak operation mode is extending in collisionality, high edge density, q_{95} ranging from 3 to 5, non-inductive current drive fractions above 50%, and operating with a high-Z first wall. In terms of the scenario recipe a flat central q-profile with q≈1 is favourable with clamping of the current profile provided by fishbones (higher performance). Within the European

discussion the improved H-mode is evolving as the reference for the 'conservative' DEMO concept.
The tungsten wall programme is as important for DEMO as the erosion of low-Z material and the destruction of graphite under neutron bombardment will be unacceptable there. The full W coverage will give decisive answers for high-Z operation where sputtering due to the ICRH accelerated impurity ions at the antenna limiters remain a problem. In summary, AUG plays an essential role in the design of ITER and preparation of ITER operation, and its role in the preparation of the DEMO concept is growing.

References

[1] ITER Physics Basis 1999 Nucl. Fusion **39** 2137
[2] Raupp G. et al., 10th ICALEPS, Geneva (2005) 10-10 to 10-14
[3] Raupp G. et al, Fus. Eng.and Design 74 (2005) 697
[4] Leuterer F. et al., Fus. Eng.and Design 74 (2005) 199
[5] Gruber O et al., Phys. Rev. Lett. 83 (1999) 1787
[6] Angioni C. et al, this conference, IAEA-CN-149/EX/8-5Rb
[7] Ryter F. et al., Nucl. Fusion 43 (2003) 1396
[8] Ryter F. et al, Phys. Rev. Lett. 95 (2005) 085001, and inv. EPS 2006 (to be published in PPCF (2006))
[9] Peeters A.G. et al, Phys. Plasmas 12 (2005) 022505
[10] Angioni C. et al, Phys. Rev. Lett. 90 (2003) 205003
[11] Weisen H. et al, this conference, IAEA-CN-149/EX/8-4
[12] Angioni C. et al, Nucl. Fusion 44 (2004) 827
[13] Dannert T., Jenko F. Phys. Plasmas 12 (2005) 072309
[14] Angioni C. et al, Phys. Plasmas 12 (2005) 112310
[15] Angioni C. et al, Phys. Plasmas 12 (2005) 040701
[16] Conway G.D., et al, Nucl. Fusion 46 (2006) S799
[17] Manini A. et al, 2004 Plasma Phys. Contr. Fusion 46 (2004) 1723 and Nucl. Fusion (2006) subm.
[18] Nishijima D. et al., Plasma Phys. Contr. Fusion 47 (2003) 89
[19] Peeters A.G. et al., Phys Plasmas 12 (2005) 072515
[20] Neu R. et al, J. Nucl. Mater. 116 (2003) 313
[21] Angioni C., Peeters A.G. Phys. Rev. Lett. 96 (2006) 095003
[22] Dux R., et al., Fusion Tech. 44 (2003) 708
[23] Neu R., et al., Nucl. Fusion 45 (2005) 209
[24] Conway G.D. et al., this conference, IAEA-CN-149/EX/2-1
[25] Conway G.D. et al., Plasma Phys. Control. Fusion 46 (2004) 951
[26] Schirmer J. et al., Nucl. Fusion 46 (2006) S780
[27] Conway G.D. et al., Plasma Phys. Control. Fusion 47 (2005) 1165
[28] Federici G., et al., Plasma Phys. Contr. Fusion 45 (2003) 1523
[29] Urano H. et al., Plasma Phys.Contr.Fusion 45 (2003) 1571
[30] Horton L.D., et al., Nucl. Fusion 45 (2005) 856
[31] Suttrop W. et al., this conference, IAEA-CN-149/EX/8-5
[32] Stober J. et al., Nucl. Fusion 41 (2001) 1535
[33] Gruber O. et al., 19th IAEA Conf.Fusion Energy, Lyon (2002), IAEA-CN-94/EX/C2-1
[34] Lang P.T., et al., Nucl. Fusion 44 (2004) 665
[35] Günter S. et al., Nucl. Fusion 45 (2005) S98
[36] Lang P.T., et al., Nucl. Fusion 45 (2005) 502
[37] Neuhauser J. et al., this conference, IAEA-CN-149/EX/P8-2
[38] Lang P.T., et al., Plasma Phys. Controlled Fusion 48 (2006) A141
[39] Müller H.W., et al., 29th EPS conf., Montreux (Switzerland), ECA 26B (2002) O-2.06
[40] Kurzan B. et al., Phys. Rev.Lett. 95 (2005) 145001
[41] Eich T. et al., Phys. Rev. Lett. 91 (2003) 195003 and Plasma Phys. Contr. Fusion 47 (2005) 815
[42] Herrmann A., et al., 17th PSI conf., Hefei (China), J.Nucl.Mater. subm.
[43] Kirk A. et al., Plasma Phys. Contr. Fusion 47 (2005) 995
[44] Herrmann, A. et al., Plasma Phys. Contr. Fusion 46 (2004) 971
[45] Wilson H.R., Cowley S.C., et al., Phys. Rev. Lett., 92 (2004) 175006
[46] Günter S. et al., this conference, IAEA-CN-149/EX/6-1
[47] Fasoli A. Jaun A., Testa D., Phys. Lett. A 265, 288 (2000)
[48] Lauber Ph., Günter S., Pinches S., Phys. Plasmas 12, 122501 (2005)
[49] Da Graca S. et al., 33th EPS conference, Rome, 2006, P2.146
[50] Garcia-Munoz M. et al., 32nd EPS conference, Tarragona, 2005, P-5.085
[51] Sassenberg et al., 33th EPS conference, Rome, 2006, P
[52] McCarthy P.J. et al., this conference, IAEA-CN-149/
[53] Zohm H. et al., Nucl. Fusion 39 (1999) 577
[54] Günter S. et al., Phys.Rev. Lett. 87 (2001) 275001
[55] Maraschek M. et al., Nucl. Fusion 45 (2005) 1369.
[56] Zohm H. et al., this conference, IAEA-CN-149/EX/
[57] Maraschek M. et al., submitted to Phys. Rev. Lett.

[58] La Haye R.J. et al., this conference, IAEA_CN-149/IT/
[59] Manini A. et al., to appear in Fusion Engineering and Design (2006)
[60] Pautasso G. et al., this conference, IAEA-CN-149/EX/P8-7
[61] Pautasso G. et al., Fusion Science and Technology 44 (2003) 716
[62] Pautasso G. et al., 32nd EPS conference, Tarragona, 2005, P4.074
[63] Hollmann E.M. et al., 33th EPS conference, Rome, 2006, P5.136
[64] Janeschitz G. et al, J. Nucl. Mater. 1 (2001) 290
[65] Bolt H. et al., J. Nucl. Mater. 43 (2002) 119
[66] Neu R. et al., 17. Int. Conf. on PSI 2006, Hefei, to appear in J. Nucl. Mater.
[67] Dux R. et al., this conference, IAEA-CN-149/EX/3-3Ra
[68] Kallenbach A. et al., 17. Int. Conf. on PSI 2006, Hefei, to appear in J. Nucl. Mater.
[69] Kallenbach A. et al., J. Nucl. Mater. 732 (2005) 337
[70] Dux R. et al., 17. Int. Conf. on PSI 2006, Hefei, to appear in J. Nucl. Mater.
[71] Bobkov V. et al., 17. Int. Conf. on PSI 2006, Hefei, to appear in J. Nucl. Mater.
[72] Schmid K. et al., this conference, IAEA-CN-149/EX/3-3Rb
[73] Rohde V. et al., 17. Int. Conf. on PSI 2006, Hefei, to appear in J. Nucl. Mater.
[74] Sips A.C. et al, Plasma Phys. Control. Fusion 44 (2002)B69
[75] Stäbler A. et al., Nucl. Fusion 45 (2005) 617
[76] Gruber O. et al, Plasma Phys. Control. Fusion 47 (2005)B135
[77] Luce T. .et al., Nucl. Fusion 45 (2005) S86
[79] Stober J. et al., this conference, IAEA-CN-149/EX/P1-7
[80] Suttrop W. et al., Plasma Phys. Contr. Fusion 42 (2000) A97
[81] Tardini, G. et al., Nucl. Fusion 42 (2002) 258
[82] Peeters A.G. et al., Nucl. Fusion 42 (2002) 1376
[83] Na Y.-S. et al., Nucl. Fusion 46 (2006) 232
[84] Horton L. D. et al., 33rd EPS conference, Rome (2006), P2.140
[85] Maggi C.F. et al., this conference, IAEA-CN-149/IT/P1-6
[86] Sips A.C. et al., this conference, IAEA-CN-149/EX/1-1
[87] Petty G. et al 2003 Fusion Sci. Technol. 43 (2003) 1
[88] Cordey J.G. et al 2005 Nucl. Fusion 45 (2005) 1078

ASDEX Upgrade Team

C. Angioni[1], C.V. Atanasiu[2], M. Balden[1], G. Becker[1], W. Becker[1], K. Behler[1], K. Behringer[1], A. Bergmann[1], T. Bertoncelli[1], R. Bilato[1], V. Bobkov[1], T. Bolzonella[3], A. Bottino[1], M. Brambilla[1], F. Braun[1], A. Buhler[1], A. Chankin[1], G. Conway[1], D.P. Coster[1], T. Dannert[1], S. Dietrich[1], K. Dimova[1], R. Drube[1], R. Dux[1], T. Eich[1], K. Engelhardt[1], H.-U. Fahrbach[1], U. Fantz[1], L. Fattorini[4], R. Fischer[1], A. Flaws[1], M. Foley[5], C. Forest[6], P. Franzen[1], J.C. Fuchs[1], K. Gál[7], G. Gantenbein[8], M. García Muñoz[1], L. Giannone[1], S. Gori[1], S. da Graça[1], H. Greuner[1], O. Gruber[1], S. Günter[1], G. Haas[1], J. Harhausen[1], B. Heinemann[1], A. Herrmann[1], J. Hobirk[1], D. Holtum[1], L. Horton[1], M. Huart[1], V. Igochine[1], A. Jacchia[9], F. Jenko[1], A. Kallenbach[1], S. Kálvin[7], O. Kardaun[1], M. Kaufmann[1], M. Kick[1], G. Koscis[7], H. Kollotzek[1], C. Konz[1], K. Krieger[1], H. Kroiss[1], T. Kubach[8], T. Kurki-Suonio[10], B. Kurzan[1], K. Lackner[1], P.T. Lang[1], P. Lauber[1], M. Laux[1], F. Leuterer[1], J. Likonen[11], A. Lohs[1], A. Lyssoivan[12], C. Maggi[1], H. Maier[1], K. Mank[1], A. Manini[1], M.-E. Manso[4], P. Mantica[9], M. Maraschek[1], P. Martin[3], M. Mayer[1], P. McCarthy[5], H. Meister[1], F. Meo[13], P. Merkel[1], R. Merkel[1], V. Mertens[1], F. Merz[1], H. Meyer[14], F. Monaco[1], H.-W. Müller[1], M. Münich[1], H. Murmann[1], Y.-S. Na[1], G. Neu[1], R. Neu[1], J. Neuhauser[1], J.-M. Noterdaeme[1], M. Pacco-Düchs[1], G. Pautasso[1], A.G. Peeters[1], G. Pereverzev[1], S. Pinches[1], E. Poli[1], M. Püschel[1], T. Pütterich[1], R. Pugno[1], E. Quigley[5], I. Radivojevic[1], G. Raupp[1], M. Reich[1], T. Ribeiro[4], R. Riedl[1], V. Rohde[1], J. Roth[1], M. Rott[1], F. Ryter[1], W. Sandmann[1], J. Santos[4], K. Sassenberg[5], G. Schall[1], H.-B. Schilling[1], J. Schirmer[1], A. Schmid[1], W. Schneider[1], G. Schramm[1], W. Schustereder[15], J. Schweinzer[1], S. Schweizer[1], B. Scott[1], U. Seidel[1], M. Serbu[1], F. Serra[4], Y. Shi[16], A. Silva[4], A.C.C. Sips[1], E. Speth[1], A. Stäbler[1], K.-H. Steuer[1], J. Stober[1], B. Streibl[1], D. Strintzi[1], E. Strumberger[1], W. Suttrop[1], G. Tardini[1], C. Tichmann[1], W. Treutterer[1], C. Tröster[1], M. Tsalas[17], L. Urso[1], E. Vainonen-Ahlgren[11], P. Varela[4], L. Vermare[1], D. Wagner[1], M. Wischmeier[1], E. Wolfrum[1], E. Würsching[1], Q. Yu[1], D. Zasche[1], T. Zehetbauer[1], M. Zilker[1], H. Zohm[1].

[1] Max-Planck-Institut für Plasmaphysik, EURATOM Association-IPP, 85748 Garching, Germany
[2] Institute of Atomic Physics, EURATOM Association-MEdC, Romania, [3] Consorzio RFX, EURATOM Association-ENEA, Padova, Italy, [4] CFN, EURATOM Association-IST Lisbon, Portugal, [5] Physics Dep., University College Cork, Association EURATOM-DCU, Ireland, [6] University of Wisconsin, Madison, USA. [7] KFKI, EURATOM Association-HAS, Budapest, Hungary, [8] Institut für Plasmaforschung, Stuttgart University, Germany, [9] IFP Milano, EURATOM Association-ENEA, Italy, [10] HUT, EURATOM Association-Tekes, Helsinki, Finland, [11] VTT, EURATOM Association-Tekes, Espoo, Finland, [12] LPP-ERM/KMS, EURATOM Association-Belgian State, Brussels, Belgium, [13] NL Risø, EURATOM Association-RISØ, Roskilde, Denmark, [14] UKAEA Culham, EURATOM Association-UKAEA, United Kingdom, [15] University of Innsbruck, EURATOM Association-ÖAW, Austria [16] IPP, CAS, Hefei, China, [17] NCSR Demokritos, EURATOM Association-HELLAS, Athens, Greece